

Search for a Higgs boson in diphoton final states with the D0 detector in 9.6 fb^{-1} of $p\bar{p}$ collisions at $\sqrt{s} = 1.96 \text{ TeV}$

V. M. Abazov,³² B. Abbott,⁶⁷ B. S. Acharya,²⁶ M. Adams,⁴⁶ T. Adams,⁴⁴ G. D. Alexeev,³² G. Alkhalaf,³⁶ A. Alton,^{56,*} A. Askew,⁴⁴ S. Atkins,⁵⁴ K. Augsten,⁷ C. Avila,⁵ F. Badaud,¹⁰ L. Bagby,⁴⁵ B. Baldin,⁴⁵ D. V. Bandurin,⁴⁴ S. Banerjee,²⁶ E. Barberis,⁵⁵ P. Baringer,⁵³ J. F. Bartlett,⁴⁵ U. Bassler,¹⁵ V. Bazterra,⁴⁶ A. Bean,⁵³ M. Begalli,² L. Bellantoni,⁴⁵ S. B. Beri,²⁴ G. Bernardi,¹⁴ R. Bernhard,¹⁹ I. Bertram,³⁹ M. Besançon,¹⁵ R. Beuselinck,⁴⁰ P. C. Bhat,⁴⁵ S. Bhatia,⁵⁸ V. Bhatnagar,²⁴ G. Blazey,⁴⁷ S. Blessing,⁴⁴ K. Bloom,⁵⁹ A. Boehnlein,⁴⁵ D. Boline,⁶⁴ E. E. Boos,³⁴ G. Borissov,³⁹ A. Brandt,⁷⁰ O. Brandt,²⁰ R. Brock,⁵⁷ A. Bross,⁴⁵ D. Brown,¹⁴ X. B. Bu,⁴⁵ M. Buehler,⁴⁵ V. Buescher,²¹ V. Bunichev,³⁴ S. Burdin,^{39,†} C. P. Buszello,³⁸ E. Camacho-Pérez,²⁹ B. C. K. Casey,⁴⁵ H. Castilla-Valdez,²⁹ S. Caughron,⁵⁷ S. Chakrabarti,⁶⁴ D. Chakraborty,⁴⁷ K. M. Chan,⁵¹ A. Chandra,⁷² E. Chapon,¹⁵ G. Chen,⁵³ S. W. Cho,²⁸ S. Choi,²⁸ B. Choudhary,²⁵ S. Cihangir,⁴⁵ D. Claes,⁵⁹ J. Clutter,⁵³ M. Cooke,⁴⁵ W. E. Cooper,⁴⁵ M. Corcoran,⁷² F. Couderc,¹⁵ M.-C. Cousinou,¹² D. Cutts,⁶⁹ A. Das,⁴² G. Davies,⁴⁰ S. J. de Jong,^{30,31} E. De La Cruz-Burelo,²⁹ F. Déliot,¹⁵ R. Demina,⁶³ D. Denisov,⁴⁵ S. P. Denisov,³⁵ S. Desai,⁴⁵ C. Deterre,^{20,§} K. DeVaughan,⁵⁹ H. T. Diehl,⁴⁵ M. Diesburg,⁴⁵ P. F. Ding,⁴¹ A. Dominguez,⁵⁹ A. Dubey,²⁵ L. V. Dudko,³⁴ A. Duperrin,¹² S. Dutt,²⁴ A. Dyshkant,⁴⁷ M. Eads,⁴⁷ D. Edmunds,⁵⁷ J. Ellison,⁴³ V. D. Elvira,⁴⁵ Y. Enari,¹⁴ H. Evans,⁴⁹ V. N. Evdokimov,³⁵ L. Feng,⁴⁷ T. Ferbel,⁶³ F. Fiedler,²¹ F. Filthaut,^{30,31} W. Fisher,⁵⁷ H. E. Fisk,⁴⁵ M. Fortner,⁴⁷ H. Fox,³⁹ S. Fuess,⁴⁵ A. Garcia-Bellido,⁶³ J. A. García-González,²⁹ G. A. García-Guerra,^{29,‡} V. Gavrilov,³³ W. Geng,^{12,57} C. E. Gerber,⁴⁶ Y. Gershtein,⁶⁰ G. Ginther,^{45,63} G. Golovanov,³² P. D. Grannis,⁶⁴ S. Greder,¹⁶ H. Greenlee,⁴⁵ G. Grenier,¹⁷ Ph. Gris,¹⁰ J.-F. Grivaz,¹³ A. Grohsjean,^{15,§} S. Grünendahl,⁴⁵ M. W. Grünewald,²⁷ T. Guillemain,¹³ G. Gutierrez,⁴⁵ P. Gutierrez,⁶⁷ J. Haley,⁵⁵ L. Han,⁴ K. Harder,⁴¹ A. Harel,⁶³ J. M. Hauptman,⁵² J. Hays,⁴⁰ T. Head,⁴¹ T. Hebbeker,¹⁸ D. Hedin,⁴⁷ H. Hegab,⁶⁸ A. P. Heinson,⁴³ U. Heintz,⁶⁹ C. Hensel,²⁰ I. Heredia-De La Cruz,²⁹ K. Herner,⁵⁶ G. Hesketh,^{41,||} M. D. Hildreth,⁵¹ R. Hirosky,⁷³ T. Hoang,⁴⁴ J. D. Hobbs,⁶⁴ B. Hoeneisen,⁹ J. Hogan,⁷² M. Hohlfeld,²¹ I. Howley,⁷⁰ Z. Hubacek,^{7,15} V. Hynek,⁷ I. Iashvili,⁶² Y. Ilchenko,⁷¹ R. Illingworth,⁴⁵ A. S. Ito,⁴⁵ S. Jabeen,⁶⁹ M. Jaffré,¹³ A. Jayasinghe,⁶⁷ M. S. Jeong,²⁸ R. Jesik,⁴⁰ P. Jiang,⁴ K. Johns,⁴² E. Johnson,⁵⁷ M. Johnson,⁴⁵ A. Jonckheere,⁴⁵ P. Jonsson,⁴⁰ J. Joshi,⁴³ A. W. Jung,⁴⁵ A. Juste,³⁷ E. Kajfasz,¹² D. Karmanov,³⁴ I. Katsanos,⁵⁹ R. Kehoe,⁷¹ S. Kermiche,¹² N. Khalatyan,⁴⁵ A. Khanov,⁶⁸ A. Kharchilava,⁶² Y. N. Kharzhev,³² I. Kiselevich,³³ J. M. Kohli,²⁴ A. V. Kozelov,³⁵ J. Kraus,⁵⁸ A. Kumar,⁶² A. Kupco,⁸ T. Kurča,¹⁷ V. A. Kuzmin,³⁴ S. Lammers,⁴⁹ P. Lebrun,¹⁷ H. S. Lee,²⁸ S. W. Lee,⁵² W. M. Lee,⁴⁴ X. Lei,⁴² J. Lellouch,¹⁴ D. Li,¹⁴ H. Li,⁷³ L. Li,⁴³ Q. Z. Li,⁴⁵ J. K. Lim,²⁸ D. Lincoln,⁴⁵ J. Linnemann,⁵⁷ V. V. Lipaev,³⁵ R. Lipton,⁴⁵ H. Liu,⁷¹ Y. Liu,⁴ A. Lobodenko,³⁶ M. Lokajicek,⁸ R. Lopes de Sa,⁶⁴ R. Luna-Garcia,^{29,**} A. L. Lyon,⁴⁵ A. K. A. Maciel,¹ R. Magaña-Villalba,²⁹ S. Malik,⁵⁹ V. L. Malyshev,³² J. Mansour,²⁰ J. Martínez-Ortega,²⁹ R. McCarthy,⁶⁴ C. L. McGivern,⁴¹ M. M. Meijer,^{30,31} A. Melnitchouk,⁴⁵ D. Menezes,⁴⁷ P. G. Mercadante,³ M. Merkin,³⁴ A. Meyer,¹⁸ J. Meyer,^{20,§§} F. Miconi,¹⁶ N. K. Mondal,²⁶ M. Mulhearn,⁷³ E. Nagy,¹² M. Naimuddin,²⁵ M. Narain,⁶⁹ R. Nayyar,⁴² H. A. Neal,⁵⁶ J. P. Negret,⁵ P. Neustroev,³⁶ H. T. Nguyen,⁷³ T. Nunnemann,²² J. Orduna,⁷² N. Osman,¹² J. Osta,⁵¹ M. Padilla,⁴³ A. Pal,⁷⁰ N. Parashar,⁵⁰ V. Parihar,⁶⁹ S. K. Park,²⁸ R. Partridge,^{69,||} N. Parua,⁴⁹ A. Patwa,^{65,|||} B. Penning,⁴⁵ M. Perfilov,³⁴ Y. Peters,²⁰ K. Petridis,⁴¹ G. Petrillo,⁶³ P. Pétroff,¹³ M.-A. Pleier,⁶⁵ P. L. M. Podesta-Lerma,^{29,††} V. M. Podstavkov,⁴⁵ A. V. Popov,³⁵ M. Prewitt,⁷² D. Price,⁴⁹ N. Prokopenko,³⁵ J. Qian,⁵⁶ A. Quadt,²⁰ B. Quinn,⁵⁸ M. S. Rangel,¹ P. N. Ratoff,³⁹ I. Razumov,³⁵ I. Ripp-Baudot,¹⁶ F. Rizatdinova,⁶⁸ M. Rominsky,⁴⁵ A. Ross,³⁹ C. Royon,¹⁵ P. Rubinov,⁴⁵ R. Ruchti,⁵¹ G. Sajot,¹¹ P. Salcido,⁴⁷ A. Sánchez-Hernández,²⁹ M. P. Sanders,²² A. S. Santos,^{1,‡‡} G. Savage,⁴⁵ L. Sawyer,⁵⁴ T. Scanlon,⁴⁰ R. D. Schamberger,⁶⁴ Y. Scheglov,³⁶ H. Schellman,⁴⁸ C. Schwanenberger,⁴¹ R. Schwienhorst,⁵⁷ J. Sekaric,⁵³ H. Severini,⁶⁷ E. Shabalina,²⁰ V. Shary,¹⁵ S. Shaw,⁵⁷ A. A. Shchukin,³⁵ R. K. Shivpuri,²⁵ V. Simak,⁷ P. Skubic,⁶⁷ P. Slattery,⁶³ D. Smirnov,⁵¹ K. J. Smith,⁶² G. R. Snow,⁵⁹ J. Snow,⁶⁶ S. Snyder,⁶⁵ S. Söldner-Rembold,⁴¹ L. Sonnenschein,¹⁸ K. Soustruznik,⁶ J. Stark,¹¹ D. A. Stoyanova,³⁵ M. Strauss,⁶⁷ L. Suter,⁴¹ P. Svoisky,⁶⁷ M. Titov,¹⁵ V. V. Tokmenin,³² Y.-T. Tsai,⁶³ D. Tsybychev,⁶⁴ B. Tuchming,¹⁵ C. Tully,⁶¹ L. Uvarov,³⁶ S. Uvarov,³⁶ S. Uzunyan,⁴⁷ R. Van Kooten,⁴⁹ W. M. van Leeuwen,³⁰ N. Varelas,⁴⁶ E. W. Varnes,⁴² I. A. Vasilyev,³⁵ A. Y. Verkheev,³² L. S. Vertogradov,³² M. Verzocchi,⁴⁵ M. Vesterinen,⁴¹ D. Vilanova,¹⁵ P. Vokac,⁷ H. D. Wahl,⁴⁴ M. H. L. S. Wang,⁴⁵ J. Warchol,⁵¹ G. Watts,⁷⁴ M. Wayne,⁵¹ J. Weichert,²¹ L. Welty-Rieger,⁴⁸ A. White,⁷⁰ D. Wicke,²³ M. R. J. Williams,³⁹ G. W. Wilson,⁵³ M. Wobisch,⁵⁴ D. R. Wood,⁵⁵ T. R. Wyatt,⁴¹ Y. Xie,⁴⁵ R. Yamada,⁴⁵ S. Yang,⁴ T. Yasuda,⁴⁵ Y. A. Yatsunenko,³² W. Ye,⁶⁴ Z. Ye,⁴⁵ H. Yin,⁴⁵ K. Yip,⁶⁵ S. W. Youn,⁴⁵ J. M. Yu,⁵⁶ J. Zennaro,⁶² T. G. Zhao,⁴¹ B. Zhou,⁵⁶ J. Zhu,⁵⁶ M. Zielinski,⁶³ D. Zieminska,⁴⁹ and L. Zivkovic¹⁴

(D0 Collaboration)

- ¹LAFEX, Centro Brasileiro de Pesquisas Físicas, Rio de Janeiro, Brazil
²Universidade do Estado do Rio de Janeiro, Rio de Janeiro, Brazil
³Universidade Federal do ABC, Santo André, Brazil
⁴University of Science and Technology of China, Hefei, People's Republic of China
⁵Universidad de los Andes, Bogotá, Colombia
⁶Charles University, Faculty of Mathematics and Physics, Center for Particle Physics, Prague, Czech Republic
⁷Czech Technical University in Prague, Prague, Czech Republic
⁸Center for Particle Physics, Institute of Physics, Academy of Sciences of the Czech Republic, Prague, Czech Republic
⁹Universidad San Francisco de Quito, Quito, Ecuador
¹⁰LPC, Université Blaise Pascal, CNRS/IN2P3, Clermont, France
¹¹LPSC, Université Joseph Fourier Grenoble 1, CNRS/IN2P3, Institut National Polytechnique de Grenoble, Grenoble, France
¹²CPPM, Aix-Marseille Université, CNRS/IN2P3, Marseille, France
¹³LAL, Université Paris-Sud, CNRS/IN2P3, Orsay, France
¹⁴LPNHE, Universités Paris VI and VII, CNRS/IN2P3, Paris, France
¹⁵CEA, Irfu, SPP, Saclay, France
¹⁶IPHC, Université de Strasbourg, CNRS/IN2P3, Strasbourg, France
¹⁷IPNL, Université Lyon 1, CNRS/IN2P3, Villeurbanne, France and Université de Lyon, Lyon, France
¹⁸III. Physikalisches Institut A, RWTH Aachen University, Aachen, Germany
¹⁹Physikalisches Institut, Universität Freiburg, Freiburg, Germany
²⁰II. Physikalisches Institut, Georg-August-Universität Göttingen, Göttingen, Germany
²¹Institut für Physik, Universität Mainz, Mainz, Germany
²²Ludwig-Maximilians-Universität München, München, Germany
²³Fachbereich Physik, Bergische Universität Wuppertal, Wuppertal, Germany
²⁴Panjab University, Chandigarh, India
²⁵Delhi University, Delhi, India
²⁶Tata Institute of Fundamental Research, Mumbai, India
²⁷University College Dublin, Dublin, Ireland
²⁸Korea Detector Laboratory, Korea University, Seoul, Korea
²⁹CINVESTAV, Mexico City, Mexico
³⁰Nikhef, Science Park, Amsterdam, The Netherlands
³¹Radboud University Nijmegen, Nijmegen, The Netherlands
³²Joint Institute for Nuclear Research, Dubna, Russia
³³Institute for Theoretical and Experimental Physics, Moscow, Russia
³⁴Moscow State University, Moscow, Russia
³⁵Institute for High Energy Physics, Protvino, Russia
³⁶Petersburg Nuclear Physics Institute, St. Petersburg, Russia
³⁷Institució Catalana de Recerca i Estudis Avançats (ICREA) and Institut de Física d'Altes Energies (IFAE), Barcelona, Spain
³⁸Uppsala University, Uppsala, Sweden
³⁹Lancaster University, Lancaster LA1 4YB, United Kingdom
⁴⁰Imperial College London, London SW7 2AZ, United Kingdom
⁴¹The University of Manchester, Manchester M13 9PL, United Kingdom
⁴²University of Arizona, Tucson, Arizona 85721, USA
⁴³University of California Riverside, Riverside, California 92521, USA
⁴⁴Florida State University, Tallahassee, Florida 32306, USA
⁴⁵Fermi National Accelerator Laboratory, Batavia, Illinois 60510, USA
⁴⁶University of Illinois at Chicago, Chicago, Illinois 60607, USA
⁴⁷Northern Illinois University, DeKalb, Illinois 60115, USA
⁴⁸Northwestern University, Evanston, Illinois 60208, USA
⁴⁹Indiana University, Bloomington, Indiana 47405, USA
⁵⁰Purdue University Calumet, Hammond, Indiana 46323, USA
⁵¹University of Notre Dame, Notre Dame, Indiana 46556, USA
⁵²Iowa State University, Ames, Iowa 50011, USA
⁵³University of Kansas, Lawrence, Kansas 66045, USA
⁵⁴Louisiana Tech University, Ruston, Louisiana 71272, USA
⁵⁵Northeastern University, Boston, Massachusetts 02115, USA
⁵⁶University of Michigan, Ann Arbor, Michigan 48109, USA
⁵⁷Michigan State University, East Lansing, Michigan 48824, USA

- ⁵⁸University of Mississippi, University, Mississippi 38677, USA
⁵⁹University of Nebraska, Lincoln, Nebraska 68588, USA
⁶⁰Rutgers University, Piscataway, New Jersey 08855, USA
⁶¹Princeton University, Princeton, New Jersey 08544, USA
⁶²State University of New York, Buffalo, New York 14260, USA
⁶³University of Rochester, Rochester, New York 14627, USA
⁶⁴State University of New York, Stony Brook, New York 11794, USA
⁶⁵Brookhaven National Laboratory, Upton, New York 11973, USA
⁶⁶Langston University, Langston, Oklahoma 73050, USA
⁶⁷University of Oklahoma, Norman, Oklahoma 73019, USA
⁶⁸Oklahoma State University, Stillwater, Oklahoma 74078, USA
⁶⁹Brown University, Providence, Rhode Island 02912, USA
⁷⁰University of Texas, Arlington, Texas 76019, USA
⁷¹Southern Methodist University, Dallas, Texas 75275, USA
⁷²Rice University, Houston, Texas 77005, USA
⁷³University of Virginia, Charlottesville, Virginia 22904, USA
⁷⁴University of Washington, Seattle, Washington 98195, USA
(Received 25 January 2013; published 17 September 2013)

We present a search for a Higgs boson decaying into a pair of photons based on 9.6 fb^{-1} of $p\bar{p}$ collisions at $\sqrt{s} = 1.96 \text{ TeV}$ collected with the D0 detector at the Fermilab Tevatron Collider. The search employs multivariate techniques to discriminate signal from the nonresonant background and is separately optimized for a standard model and a fermiophobic Higgs boson. No significant excess of data above the background prediction is observed and upper limits on the product of the cross section and branching fraction are derived at the 95% confidence level as a function of Higgs boson mass. For a standard model Higgs boson with mass of 125 GeV, the observed (expected) upper limits are a factor of 12.8 (8.7) above the standard model prediction. The existence of a fermiophobic Higgs boson with mass in the 100–113 GeV range is excluded at the 95% confidence level.

DOI: [10.1103/PhysRevD.88.052007](https://doi.org/10.1103/PhysRevD.88.052007)

PACS numbers: 14.80.Bn, 12.60.Fr, 13.85.Rm, 14.80.Ec

I. INTRODUCTION

Unraveling the mechanism for electroweak symmetry breaking and the generation of mass of elementary particles has been a priority in experimental particle physics research during the last decades. In the standard model (SM) [1] this is accomplished by introducing a SU(2) doublet of self-interacting elementary scalars, the ‘‘Higgs field,’’ whose nonzero vacuum expectation value breaks the electroweak symmetry and generates the mass of the W and Z bosons [2]. The postulated Yukawa interactions between the fermions and the Higgs field also gives mass

to fermions upon the breaking of the electroweak symmetry. Furthermore, a physical scalar particle appears in the spectrum, the Higgs boson (H), whose mass is not predicted and must be determined experimentally.

Within the SM, indirect constraints from precision electroweak observables [3] limit the allowed range for the Higgs boson mass (M_H) to $M_H < 152 \text{ GeV}$ at the 95% confidence level (C.L.). Direct searches at the CERN e^+e^- Collider (LEP) [4] set a lower limit of $M_H > 114.4 \text{ GeV}$ at 95% C.L. At hadron colliders the dominant production mechanisms for a SM Higgs boson are gluon fusion (GF) ($gg \rightarrow H$), associated production with a W or Z boson ($q\bar{q}' \rightarrow VH$, $V = W, Z$), and vector-boson fusion (VBF) ($VV \rightarrow H$). However, the search strategies for a light SM Higgs boson are different at the Fermilab Tevatron $p\bar{p}$ Collider and at CERN’s Large Hadron pp Collider (LHC).

At the Tevatron, the most sensitive SM Higgs boson searches for $M_H < 130 \text{ GeV}$ rely on the VH production mode, with $H \rightarrow b\bar{b}$, while for $M_H > 130 \text{ GeV}$ the main search mode is $gg \rightarrow H \rightarrow W^+W^-$. The combination of searches at the Tevatron [5] have resulted in the mass ranges $90 < M_H < 109 \text{ GeV}$ and $149 < M_H < 182 \text{ GeV}$ being excluded at the 95% C.L. In the allowed intermediate mass range an excess is found with a maximum local significance of 3.0 standard deviations (s.d.) at $M_H = 125 \text{ GeV}$, primarily originating from the VH ($H \rightarrow b\bar{b}$) searches [6]. This result constitutes an important input for

* Visitor from Augustana College, Sioux Falls, SD, USA.

† Visitor from The University of Liverpool, Liverpool, UK.

‡ Visitor from UPIITA-IPN, Mexico City, Mexico.

§ Visitor from DESY, Hamburg, Germany.

|| Visitor from SLAC, Menlo Park, CA, USA.

¶ Visitor from University College London, London, UK.

** Visitor from Centro de Investigacion en Computacion-IPN, Mexico City, Mexico.

†† Visitor from ECFM, Universidad Autonoma de Sinaloa, Culiacán, Mexico.

‡‡ Visitor from Universidade Estadual Paulista, São Paulo, Brazil.

§§ Visitor from Karlsruhe Institut für Technologie (KIT)-Steinbuch Centre for Computing (SCC).

||| Visitor from Office of Science, U.S. Department of Energy, Washington, D.C. 20585, USA.

the upcoming publications on combinations of Higgs boson searches by the D0 experiment, as well as by both Tevatron experiments, using the complete Run II data set [5].

At the LHC, the search strategy for $M_H > 140$ GeV also capitalizes on the GF production mode, exploiting primarily the $H \rightarrow W^+W^-$ and $H \rightarrow ZZ$ decay modes with leptonic W - and Z -boson decays. The $H \rightarrow \gamma\gamma$ decay mode becomes one of the most promising discovery channels at lower M_H , despite its small branching fraction of $\mathcal{B}(H \rightarrow \gamma\gamma) \approx 0.2\%$, owing to its clean experimental signature of a narrow resonance on top of a smoothly falling background in the diphoton mass ($M_{\gamma\gamma}$) spectrum. Searches for $H \rightarrow ZZ^{(*)} \rightarrow \ell^+\ell^-\ell'^+\ell'^-$ ($\ell, \ell' = e, \mu$) are also sensitive due to the small background and excellent four-lepton invariant mass resolution. The most recent searches for the SM Higgs boson at the LHC [7,8] exclude a SM Higgs boson with $M_H \leq 600$ GeV, except for the narrow mass range ≈ 122 – 127 GeV. In this mass range both the ATLAS and the CMS Collaborations observe a significant excess of events in data at $M_H \approx 125$ GeV with local significances of 5.9 and 5.0 s.d., respectively. These excesses are formed by smaller excesses observed in searches focused on $H \rightarrow \gamma\gamma$ and $H \rightarrow ZZ^{(*)}$ decays, while no significant excesses have been found in searches targeting fermionic decay modes ($H \rightarrow b\bar{b}$ and $H \rightarrow \tau^+\tau^-$) with the data sets analyzed so far.

Searches for $H \rightarrow \gamma\gamma$ are particularly sensitive to new particles beyond the SM contributing to the loop-mediated Hgg and/or $H\gamma\gamma$ vertices, and to deviations in the couplings between the SM particles and the Higgs boson from those predicted by the SM. For example, alternative models of electroweak symmetry breaking [9] can involve suppressed couplings of the Higgs boson to fermions, with the extreme case being the fermiophobic Higgs boson (H_f) scenario, in which H_f has no tree-level couplings to fermions but has SM coupling to weak gauge bosons. In this scenario the GF production mechanism is absent, decays into fermions are heavily suppressed, and $\mathcal{B}(H \rightarrow \gamma\gamma)$ is significantly enhanced. The best-fit cross sections to the signal-like excesses in the $H \rightarrow \gamma\gamma$ searches at the LHC show small deviations of about 1.5 s.d. above the SM prediction [7,8]. A more detailed global fit to Higgs boson couplings [10] shows no significant deviations. Hence, the analysis of more data is needed for more definitive conclusions. Searches for a fermiophobic Higgs boson were performed by the LEP Collaborations [11], the CDF [12] and D0 [13] Collaborations and, most recently, by the ATLAS [14] and CMS [15] Collaborations. The most restrictive limits result from the combination of $H \rightarrow \gamma\gamma$, $H \rightarrow W^+W^-$ and $H \rightarrow ZZ$ searches by the CMS Collaboration, excluding the mass range $110 < M_{H_f} < 194$ GeV.

In this article, we present the result from the search for a Higgs boson decaying into $\gamma\gamma$ using the complete data set collected with the D0 detector in $p\bar{p}$ collisions at $\sqrt{s} = 1.96$ TeV during Run II of the Tevatron Collider.

This search employs multivariate techniques to improve the signal-to-background discrimination, and is separately optimized for a SM Higgs boson and for a fermiophobic Higgs boson. Compared to the previous D0 publication [13], the sensitivity for the SM Higgs boson is improved by about 40%, resulting in the most restrictive limits to date from the Tevatron in this decay mode. The search for a fermiophobic Higgs boson has comparable sensitivity with the most recent result from the CDF Collaboration [12]. This result constitutes an important input for the upcoming publications on combinations of Higgs boson searches by the D0 experiment, as well as by both Tevatron experiments, using the complete Run II data set.

II. D0 DETECTOR AND DATA SET

The D0 detector is described in detail elsewhere [16]. The subdetectors most relevant to this analysis are the central tracking system, composed of a silicon microstrip tracker (SMT) and a central fiber tracker (CFT) in a 2 T solenoidal magnetic field, the central preshower (CPS), and the liquid-argon and uranium sampling calorimeter.

The SMT has about 800 000 individual strips, with a typical pitch of 50–80 μm , and a design optimized for tracking and vertexing capability at pseudorapidities of $|\eta| < 2.5$ [17]. The system has a six-barrel longitudinal structure, each with a set of four layers arranged axially around the beam pipe, and interspersed with 16 radial disks. In the summer of 2006 an additional layer of silicon sensors was inserted at a radial distance of ≈ 16 mm from the beam axis, and the two outermost radial disks were removed. The CFT has eight thin coaxial barrels, each supporting two doublets of overlapping scintillating fibers with a diameter of 0.835 mm, one doublet being parallel to the collision axis, and the other alternating by $\pm 3^\circ$ relative to the axis. Light signals are transferred via clear fibers to visible light photon counters (VLPC) that have about 80% quantum efficiency.

The CPS is located just outside of the superconducting magnet coil (in front of the calorimetry) and is formed by one radiation length of absorber followed by several layers of extruded triangular scintillator strips that are read out using wavelength-shifting fibers and VLPCs.

The calorimeter consists of three sections housed in separate cryostats: a central calorimeter covering up to $|\eta| \approx 1.1$, and two end calorimeters extending the coverage up to $|\eta| \approx 4.2$. Each section is divided into electromagnetic (EM) layers on the inside and hadronic layers on the outside. The EM part of the calorimeter is segmented into four longitudinal layers with transverse segmentation of $\Delta\eta \times \Delta\phi = 0.1 \times 0.1$ [17], except in the third layer (EM3), where it is 0.05×0.05 . The calorimeter is well suited for a precise measurement of electron and photon energies, providing a resolution of $\approx 3.6\%$ at energies of ≈ 50 GeV.

Luminosity is measured using plastic scintillator arrays located in front of the end calorimeter cryostats, covering $2.7 < |\eta| < 4.4$. Trigger and data acquisition systems are

designed to accommodate the high luminosities of Run II. Based on preliminary information from tracking, calorimetry, and muon systems, the output of the first level of the trigger is used to limit the rate for accepted events to about 2 kHz. At the next trigger stage, with more refined information, the rate is reduced further to about 1 kHz. These first two levels of triggering rely mainly on hardware and firmware. The third and final level of the trigger, with access to all the event information, uses software algorithms and a computing farm, and reduces the output rate to about 100 Hz, which is written to tape.

This analysis uses the complete data set of $p\bar{p}$ collisions at $\sqrt{s} = 1.96$ TeV recorded with the D0 detector during Run II of the Tevatron Collider. The data are acquired using triggers requiring at least two clusters of energy in the EM calorimeter with loose shower-shape requirements and varying transverse-momentum (p_T) thresholds between 15 GeV and 25 GeV. The trigger efficiency is close to 100% for final states containing two photon candidates with $p_T > 25$ GeV. Only events for which all subdetector systems are fully operational are considered. The analyzed data set corresponds to an integrated luminosity of 9.6 fb^{-1} [18].

III. EVENT SIMULATION

Monte Carlo (MC) samples of Higgs boson signals are generated separately for the GF, VH and VBF processes using the PYTHIA [19] leading-order event generator with the CTEQ6L1 [20] parton distribution functions (PDFs). Signal samples are generated for $100 \leq M_H \leq 150$ GeV, in increments of 5 GeV. Signal samples are normalized using the next-to-next-to-leading-order (NNLO) plus next-to-next-to-leading-logarithm (NNLL) cross sections for GF [21] and NNLO for VH and VBF processes [22,23], computed with the MSTW 2008 PDF set [24]. The Higgs boson's branching fraction predictions are from HDECAY [25]. To improve the signal modeling for the GF process, the p_T of the Higgs boson is corrected to match the prediction at NNLO + NNLL accuracy by the HQT program [26]. In the case of the fermiophobic model, where the GF process is absent, the VH and VBF cross sections are normalized to the SM prediction, while the modified $H \rightarrow \gamma\gamma$ branching fractions are computed with HDECAY.

The main background affecting this search is direct photon pair (DPP) production, where two isolated photons with high transverse momenta are produced. The rest of the backgrounds are of instrumental origin and include $\gamma + \text{jet}$ (γj) and dijet (jj) production, where at least one jet is misidentified as a photon. A smaller instrumental background originates from $Z/\gamma^* \rightarrow e^+e^-$ production, where both electrons are misidentified as photons. The normalization and shape of the γj and jj backgrounds, as well as the overall normalization of the DPP background, are estimated from data, as discussed in Sec. V. The shape of the DPP background is modeled via a MC sample

generated using SHERPA [27] with the CTEQ6L1 PDF set. Recent measurements of DPP differential cross sections [28] have shown that SHERPA provides an adequate model of this process in the kinematic region of interest for this search. The $Z/\gamma^* \rightarrow e^+e^-$ process is modeled using ALPGEN [29] with the CTEQ6L1 PDF set, interfaced to PYTHIA for parton showering and hadronization, with a subsequent correction to the p_T spectrum of the Z boson to match measurements in data [30]. The $Z/\gamma^* \rightarrow e^+e^-$ MC sample is normalized to the NNLO theoretical cross section [31].

All MC samples are processed through a GEANT-based [32] simulation of the D0 detector. To accurately model the effects of multiple $p\bar{p}$ interactions and detector noise, data events from random $p\bar{p}$ crossings that have an instantaneous luminosity spectrum similar to the events in this analysis are overlaid on the MC events. These MC events are then processed using the same reconstruction algorithms as used on the data. Simulated events are corrected so that the physics object identification efficiencies, energy scales and energy resolutions match those determined in data control samples.

IV. OBJECT IDENTIFICATION AND EVENT SELECTION

A. Photon reconstruction and energy scale

Photon candidates are formed from clusters of calorimeter cells within a cone of radius $\mathcal{R} = \sqrt{(\Delta\eta)^2 + (\Delta\phi)^2} = 0.4$ around a seed tower [16]. The final cluster energy is then recalculated from the inner core with $\mathcal{R} = 0.2$. The photon candidates are selected by requiring that (i) at least 95% of the cluster energy is deposited in the EM calorimeter layers, (ii) the calorimeter isolation $I = [E_{\text{tot}}(0.4) - E_{\text{EM}}(0.2)]/E_{\text{EM}}(0.2) < 0.1$, where $E_{\text{tot}}(0.4)$ is the total energy in a cone of radius $\mathcal{R} = 0.4$ and $E_{\text{EM}}(0.2)$ is the EM energy in a cone of radius $\mathcal{R} = 0.2$, (iii) the scalar sum of the p_T of all tracks ($p_{T,\text{trk}}^{\text{sum}}$) originating from the hard-scatter $p\bar{p}$ collision vertex (see Sec. IV B) in an annulus of $0.05 < \mathcal{R} < 0.4$ around the EM cluster is less than 2 GeV, and (iv) the energy-weighted EM shower width is required to be consistent with that expected for an electromagnetic shower. This analysis only considers photon candidates with pseudorapidity $|\eta^\gamma| < 1.1$.

To suppress electrons misidentified as photons, the EM clusters are required not to be spatially matched to significant tracker activity, either a track, or a pattern of hits in the SMT and CFT consistent with that of an electron or positron trajectory [33]. In the following, this requirement will be referred to as a ‘‘track-match’’ veto.

To suppress jets misidentified as photons, an artificial neural network (NN) discriminant, which exploits differences in tracker activity and energy deposits in the calorimeter and CPS between photons and jets, is defined [34]. The photon NN is trained using diphoton and dijet MC

samples generated using PYTHIA, using the following discriminating variables: $p_{T, \text{trk}}^{\text{sum}}$, the numbers of cells above a certain threshold requirement in the first EM calorimeter layer within $\mathcal{R} < 0.2$ and within $0.2 < \mathcal{R} < 0.4$ of the EM cluster, the number of associated CPS clusters within $\mathcal{R} < 0.1$ of the EM cluster, and a measure of the width of the energy deposition in the CPS. The performance of the photon NN is verified using a data event sample consisting of photons radiated from charged leptons in Z -boson decays ($Z \rightarrow \ell^+ \ell^- \gamma$, $\ell = e, \mu$) [35]. Figure 1 compares the NN output (O_{NN}) distributions of photons and jets. The shape of the O_{NN} distribution for photons is found to be in good agreement between data and the MC simulation and is significantly different from the shape for misidentified jets. The latter is validated using a sample enriched in jets misidentified as photons as discussed in Sec. V. Photon candidates are required to have a O_{NN} value larger than 0.1, which is close to 100% efficient for photons while rejecting approximately 40% of the remaining misidentified jets.

The measured photon energies are calibrated using a two-step correction procedure. In the first step, the energy response of the calorimeter to photons is calibrated using electrons from Z -boson decays. The resulting corrections are then applied to all electromagnetic clusters. Since electrons and photons shower differently, with electrons suffering from a larger energy loss in material upstream of the calorimeter, the application of this first set of corrections results in an overestimate of the photon energy which depends on η^γ . In the second step, additional corrections are derived for photons reconstructed in the central calorimeter using a detailed GEANT-based simulation of the D0 detector response. These corrections are derived as a function of photon transverse momentum (p_T^γ) in seven intervals of η^γ : $|\eta^\gamma| < 0.4$, $0.4 \leq |\eta^\gamma| < 0.6$, $0.6 \leq |\eta^\gamma| < 0.7$, $0.7 \leq |\eta^\gamma| < 0.8$, $0.8 \leq |\eta^\gamma| < 0.9$, $0.9 \leq |\eta^\gamma| < 1.0$, and $1.0 \leq |\eta^\gamma| < 1.1$, and separately for

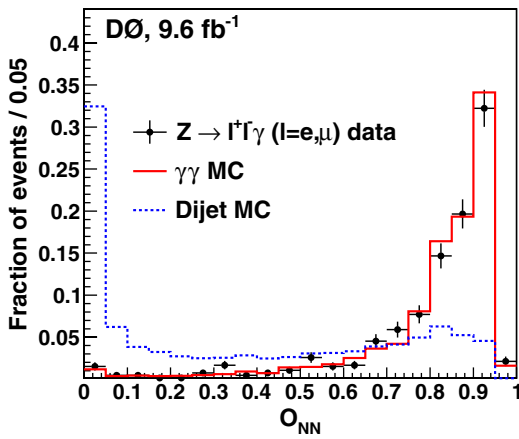


FIG. 1 (color online). Comparison of the normalized O_{NN} spectra for photons from DPP MC simulations and $Z \rightarrow \ell^+ \ell^- \gamma$ data events (points with statistical error bars), and for misidentified jets from simulated dijet events.

photons with and without a matched CPS cluster. The per-photon probability to have a matched CPS cluster is measured using photons radiated from charged leptons in Z -boson decays ($Z \rightarrow \ell^+ \ell^- \gamma$, $\ell = e, \mu$) and is $\approx 73\%$. The finer binning at higher η is motivated by the strong dependence of the energy-loss corrections for electrons on η . The resulting corrections for photons with (without) a matched CPS cluster are largest at low $p_T^\gamma \approx 20$ GeV and range from about -1.5% in the $|\eta^\gamma| < 0.4$ interval, to about -6% (-10%) in the $|\eta^\gamma| \geq 1.0$ interval.

B. Primary vertex reconstruction

At the Tevatron the distribution of $p\bar{p}$ collision vertices has a Gaussian width of about 25 cm. The proper reconstruction of the event kinematics, in particular p_T^γ and thus $M_{\gamma\gamma}$, requires the reconstruction and then correct selection of the hard-scatter $p\bar{p}$ collision primary vertex (PV) among the various candidate PVs originating from additional $p\bar{p}$ interactions.

The algorithm used for PV reconstruction is described in detail elsewhere [36]. In a first step, tracks with two or more associated SMT hits and $p_T > 0.5$ GeV are clustered along the z direction. This is followed by a Kalman Filter fit [37] to a common vertex of the tracks in each of the different vertices. Events are required to have at least one reconstructed PV with a z coordinate (z_{PV}) within 60 cm from the center of the detector, a requirement that is $\approx 98\%$ efficient.

The selection of the hard-scatter PV from the list of PV candidates with $|z_{\text{PV}}| < 60$ cm is based on an algorithm exploiting both the track multiplicity of the different vertices and the transverse and longitudinal energy distributions in the EM calorimeter and the CPS. These energy distributions allow the estimation of the photon direction and thus the z coordinate of its production vertex along the beam direction. When one or both photons reconstructed in the EM calorimeter also deposit part of their energy in the CPS, the algorithm chooses the PV whose z_{PV} is closest to the extrapolation of the photon trajectory determined from the calorimeter and the CPS information [38], provided the distance between the coordinates of the vertex and of the photon trajectory is smaller than 3 s.d. The uncertainty on this distance is dominated by the uncertainty on the extrapolation of the photon direction, which ranges from ≈ 2.5 cm for photons with $|\eta^\gamma| < 0.4$ to ≈ 4.3 cm for photons with $|\eta^\gamma| > 0.8$. Otherwise, the algorithm chooses the PV with the largest multiplicity of associated tracks.

This algorithm is optimized using $Z/\gamma^* \rightarrow e^+ e^-$ data events, where the correct hard-scatter PV associated with the reconstructed tracks is treated as corresponding to a diphoton event by ignoring the track information from the $e^+ e^-$ pair, and added to the list of PV candidates to which the selection algorithm will be applied. The fraction of $Z/\gamma^* \rightarrow e^+ e^-$ events for which the selected PV agrees with the known hard-scatter PV is shown in Fig. 2 as a

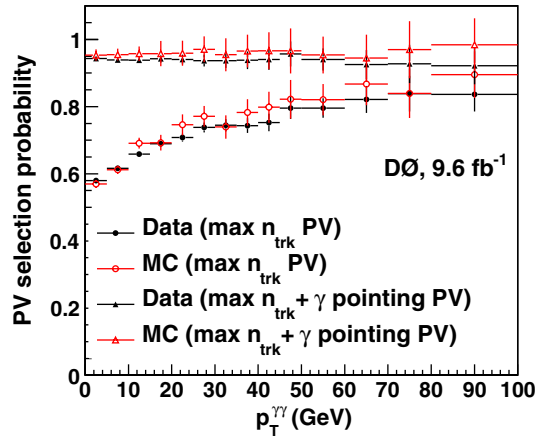


FIG. 2 (color online). Probability to select the correct hard-scatter PV as a function of $p_T^{\gamma\gamma}$ as measured in $Z/\gamma^* \rightarrow e^+e^-$ events excluding the electron and positron tracks from consideration. The two different algorithms discussed in the text are compared.

function of diphoton transverse momentum ($p_T^{\gamma\gamma}$) for two different hard-scatter PV selection algorithms. For an algorithm selecting the hard-scatter PV as the one with the highest track multiplicity, the average selection probability is only $\approx 65\%$ and shows a significant dependence on $p_T^{\gamma\gamma}$. The improved algorithm used in this analysis, including also photon pointing information, achieves an average selection probability of $\approx 95\%$, almost constant as a function of $p_T^{\gamma\gamma}$.

C. Event selection

At least two photon candidates satisfying the requirements listed in Sec. IV A and having $p_T^\gamma > 25$ GeV and $|\eta^\gamma| < 1.1$ are required. If more than two photon candidates are identified, only the two photon candidates with the highest p_T^γ are considered. At least one of the photon candidates in each event is required to have a matched CPS cluster. The photon kinematic variables are computed with respect to the vertex selected using the algorithm described in Sec. IV B. A requirement of $M_{\gamma\gamma} > 60$ GeV is made to ensure a trigger efficiency close to 100%.

The acceptance of the kinematic requirements is $\approx 42\%$, as estimated by applying the p_T^γ and η^γ requirements to generated photons in a $gg \rightarrow H \rightarrow \gamma\gamma$ MC sample assuming $M_H = 125$ GeV. At the same assumed M_H , the overall event selection efficiency, taking into account acceptance and reconstruction, identification and selection efficiencies, is $\approx 22\%$, almost independent of the signal production mechanism.

To improve the sensitivity to signal, events are categorized into two statistically independent samples with different signal-to-background ratios. Events where both photon candidates satisfy $O_{\text{NN}} > 0.75$ (“photon-enriched” sample) and events where at least one photon candidate satisfies $0.1 < O_{\text{NN}} < 0.75$ (“jet-enriched” sample) are

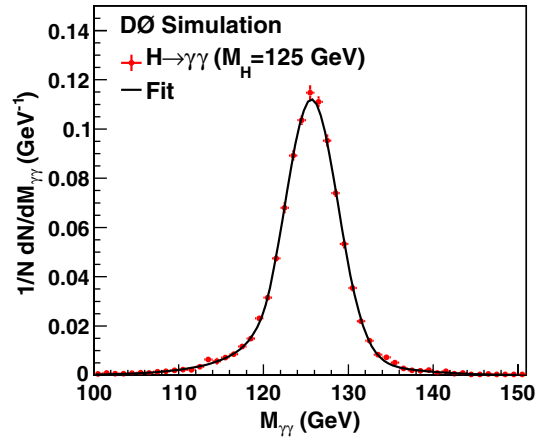


FIG. 3 (color online). Distribution of the reconstructed diphoton invariant mass distribution corresponding to a Higgs boson signal with $M_H = 125$ GeV. The line shows the result of a fit to the distribution using the functional form described in Sec. IV D.

analyzed separately. The corresponding sample compositions are discussed in Sec. V.

D. Invariant mass reconstruction

After the selection of the $p\bar{p}$ collision vertex and the photon energy scale corrections, the $M_{\gamma\gamma}$ distribution for a Higgs boson signal follows a Gaussian distribution peaking at the generated Higgs boson mass, with small non-Gaussian tails. This distribution can be modeled by the sum of a Crystal Ball function [39], describing a narrow Gaussian core and a power-law tail toward lower masses, and a wider Gaussian distribution, describing tails from misvertexing or imperfect photon energy scale corrections. Figure 3 shows such a fit to the inclusive $M_{\gamma\gamma}$ spectrum for signal MC with $M_H = 125$ GeV. The resolution of the Gaussian core is found to be ≈ 3.1 GeV, and varies by $\pm 13\%$ when varying M_H by ± 25 GeV.

V. BACKGROUND MODELING AND SAMPLE COMPOSITION

The normalization and shape of the $Z/\gamma^* \rightarrow e^+e^-$ background are estimated using simulation. Electrons are misidentified as photons at a rate of about 2% due to track reconstruction inefficiencies. Such tracking inefficiency is measured in data using a “tag-and-probe” method, where $Z \rightarrow e^+e^-$ events are selected with one of the electrons (“tag”) passing all identification criteria, including matching of the track to the calorimeter cluster, while only calorimeter requirements are applied to the other electron (“probe”). The electron misidentification rate is computed as the fraction of events where the probe electron satisfies the “track-match” veto requirement defined in Sec. IV A. The misidentification rate measured in data in this way is applied to the simulated $Z/\gamma^* \rightarrow e^+e^-$ sample.

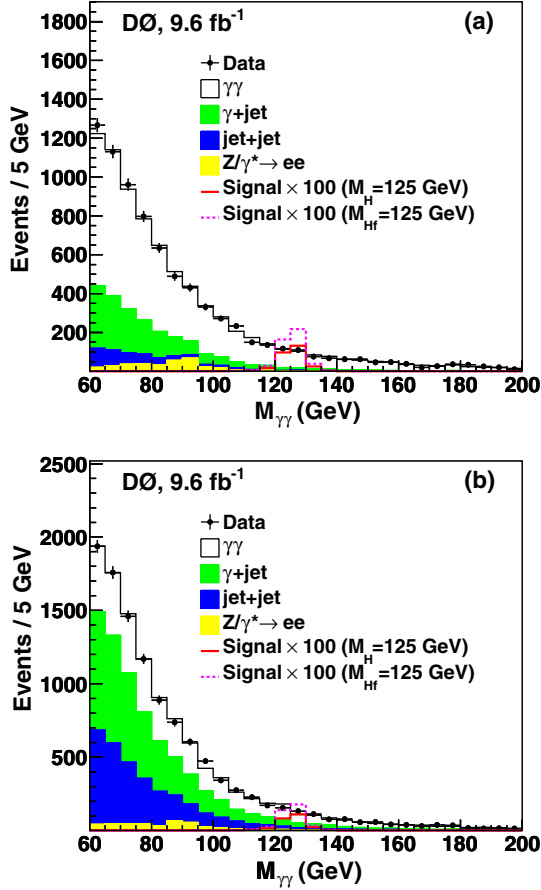


FIG. 4 (color online). Distribution of $M_{\gamma\gamma}$ in (a) the photon-enriched sample and (b) the jet-enriched sample. The data (points with statistical error bars) are compared to the background prediction, broken down into its individual components. The expected distributions for a SM Higgs boson and a fermiophobic Higgs boson with $M_H = 125$ GeV are also shown scaled by a factor of 100.

The γj and jj yields are estimated using a data-driven method [40] (“matrix method”). For selected events, the two photons are separated into two types: those with $O_{NN} > 0.75$ (well-identified photon, “p”) and those with

$0.1 < O_{NN} < 0.75$ (likely fake photon, “f”). Events are then classified in four categories: (i) two type-p photons, (ii) the higher- p_T^γ (leading) photon is type p and the lower- p_T^γ (trailing) photon is type f, (iii) the leading photon is type f and the trailing photon is type p, and (iv) two type-f photons. The corresponding numbers of events, after subtracting the $Z/\gamma^* \rightarrow e^+e^-$ contribution, are denoted as N_{pp} , N_{pf} , N_{fp} and N_{ff} . The different efficiencies of the $O_{NN} > 0.75$ requirement for photons (ϵ_γ) and jets (ϵ_j) are used to estimate the sample composition by solving a system of linear equations,

$$(N_{\gamma\gamma}, N_{\gamma j}, N_{j\gamma}, N_{jj}) = (N_{pp}, N_{pf}, N_{fp}, N_{ff}) \times \mathcal{E}^{-1}, \quad (1)$$

where $N_{\gamma\gamma}$ (N_{jj}) is the number of $\gamma\gamma$ (jj) events and $N_{\gamma j}$ ($N_{j\gamma}$) is the number of γj events with the leading (trailing) cluster as the photon. The 4×4 matrix \mathcal{E} is constructed with the efficiency terms ϵ_γ and ϵ_j , parametrized as a function of $|\eta^\gamma|$ for each photon candidate as determined from photon and jet MC samples, respectively. The ϵ_γ and ϵ_j efficiencies averaged over $|\eta^\gamma|$ are $\approx 76\%$ and $\approx 35\%$, respectively. The efficiency ϵ_γ is validated with a data sample of photons radiated from charged leptons in Z-boson decays ($Z \rightarrow \ell^+\ell^-\gamma$, $\ell = e, \mu$). The efficiency ϵ_j is validated using two independent control data samples enriched in jets misidentified as photons, either by inverting the photon isolation variable ($I > 0.1$), or by requiring at least one track in a cone of $\mathcal{R} < 0.05$ around the photon [41]. In the following, the sum of γj and $j\gamma$ contributions will be denoted as γj for simplicity. The shapes of kinematic distributions for γj (jj) background are obtained from independent control samples by requiring one (two) photon candidate(s) to satisfy $O_{NN} < 0.1$. The $O_{NN} < 0.1$ requirement leads to a mismodeling of the η^γ spectrum, due to the $|\eta^\gamma|$ dependence of ϵ_j . This is corrected by assigning a weight factor defined as $\epsilon_j(|\eta^\gamma|)/(1 - \epsilon_j(|\eta^\gamma|))$ for each of the photon candidates with $O_{NN} < 0.1$.

TABLE I. Signal, backgrounds and data yields for the photon-enriched sample within the $M_H \pm 30$ GeV mass window, for $M_H = 105$ GeV to $M_H = 145$ GeV in 10 GeV intervals. The background yields are from a fit to the data. The uncertainties include both statistical and systematic contributions added in quadrature and take into account correlations among processes. The uncertainty in the total background is smaller than the sum in quadrature of the uncertainties in the individual background sources due to the anticorrelation resulting from the fit.

M_H (GeV)	105	115	125	135	145
$\gamma\gamma$ (DPP)	2777 ± 65	1928 ± 44	1355 ± 31	980 ± 22	721 ± 17
γj	704 ± 40	407 ± 24	238 ± 14	144 ± 9	88 ± 6
jj	183 ± 16	93 ± 9	54 ± 6	34 ± 4	19 ± 2
$Z/\gamma^* \rightarrow e^+e^-$	219 ± 40	149 ± 30	51 ± 11	22 ± 5	11 ± 3
Total background	3883 ± 61	2577 ± 45	1698 ± 30	1180 ± 21	839 ± 16
Data	3777	2475	1664	1147	813
H signal	3.6 ± 0.4	3.5 ± 0.4	3.0 ± 0.4	2.2 ± 0.3	1.4 ± 0.2
H_f signal	49.8 ± 1.1	14.0 ± 0.3	4.8 ± 0.1	1.9 ± 0.1	0.79 ± 0.03

TABLE II. Signal, backgrounds and data yields for the jet-enriched sample within the $M_H \pm 30$ GeV mass window, for $M_H = 105$ GeV to $M_H = 145$ GeV in 10 GeV intervals. The background yields are from a fit to the data. The uncertainties include both statistical and systematic contributions added in quadrature and take into account correlations among processes. The uncertainty in the total background is smaller than the sum in quadrature of the uncertainties in the individual background sources due to the anticorrelation resulting from the fit.

M_H (GeV)	105	115	125	135	145
$\gamma\gamma$ (DPP)	1969 ± 47	1406 ± 33	1012 ± 24	734 ± 17	545 ± 13
γj	1852 ± 100	1101 ± 60	653 ± 36	391 ± 22	251 ± 15
jj	1188 ± 94	647 ± 54	365 ± 31	219 ± 19	135 ± 12
$Z/\gamma^* \rightarrow e^+e^-$	227 ± 39	152 ± 28	61 ± 11	30 ± 7	20 ± 5
Total background	5236 ± 67	3307 ± 45	2091 ± 29	1374 ± 21	951 ± 17
Data	5287	3384	2156	1422	989
H signal	2.7 ± 0.3	2.6 ± 0.3	2.2 ± 0.3	1.7 ± 0.2	1.1 ± 0.1
H_f signal	34.8 ± 0.8	9.8 ± 0.3	3.4 ± 0.1	1.34 ± 0.04	0.56 ± 0.02

As discussed in Sec. III, the kinematics of the DPP background are predicted using SHERPA. Since the estimated $N_{\gamma\gamma}$ from solving Eq. (1) could include a contribution from signal events, it is only used as a prior normalization for the DPP background to compare between data and background prediction. The normalization of the DPP background is ultimately determined from an unconstrained fit to the final discriminants used for hypothesis testing in both the photon-enriched and jet-enriched samples. For each of these samples, two distributions are considered: a multivariate discriminant (see Sec. VI) constructed to maximize the separation between signal and background for events with $M_{\gamma\gamma}$ falling in the interval $M_H \pm 30$ GeV (“search region”), and the $M_{\gamma\gamma}$ spectrum for events outside this interval (“sideband region”) that provide a high-statistics background-dominated sample. A comparison between data and the background prediction for the $M_{\gamma\gamma}$ spectrum, separately in the photon-enriched and the jet-enriched samples, is shown in Fig. 4.

Tables I and II summarize the number of data events, expected backgrounds, and expected SM and fermiophobic Higgs boson signals, resulting from the fit for five hypothesized Higgs boson masses, for the photon-enriched and jet-enriched samples, respectively. For $M_H = 125$ GeV, the estimated background composition for the photon-enriched sample in the $M_{\gamma\gamma}$ interval of [95 GeV, 155 GeV] is about 80% (DPP), 14% (γj), 3% (jj) and 3% ($Z/\gamma^* \rightarrow e^+e^-$). The corresponding composition for the jet-enriched sample is about 48% (DPP), 31% (γj), 18% (jj) and 3% ($Z/\gamma^* \rightarrow e^+e^-$).

VI. SIGNAL-TO-BACKGROUND DISCRIMINATION

The diphoton mass $M_{\gamma\gamma}$ is the most effective discriminating variable between the Higgs boson signal and the background. However, further discrimination can be

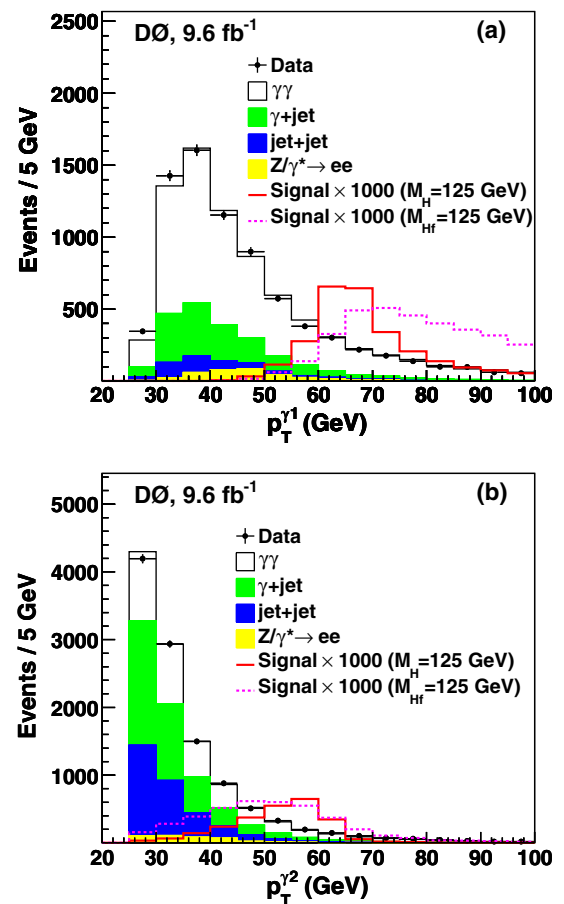


FIG. 5 (color online). Distribution of (a) $p_T^{\gamma 1}$ in the photon-enriched sample and (b) $p_T^{\gamma 2}$ in the jet-enriched sample. The data (points with statistical error bars) are compared to the background prediction, broken down into its individual components. The expected distributions for a SM Higgs boson and a fermiophobic Higgs boson with $M_H = 125$ GeV are also shown scaled by a factor of 1000. These two BDT input variables are used in both the photon-enriched and jet-enriched samples, but are displayed here for only one of the samples for illustrative purposes.

achieved by exploiting additional kinematic variables as well as photon quality variables. A total of ten well-modeled discriminating variables are considered in this search. Two of these variables correspond to kinematic properties of the photons: leading-photon transverse momentum ($p_T^{\gamma 1}$) and trailing-photon transverse momentum ($p_T^{\gamma 2}$) which, as illustrated in Fig. 5, follow a harder spectrum in signal than in background, as expected for the decay of a heavy resonance. Three of the variables are related to the kinematics of the diphoton system: $M_{\gamma\gamma}$, $p_T^{\gamma\gamma}$ and the azimuthal angle separation between the photons ($\Delta\phi_{\gamma\gamma}$). The two latter variables give discrimination due to the large p_T of the Higgs boson in VH and VBF production. Therefore, as illustrated in Fig. 6, $p_T^{\gamma\gamma}$ and $\Delta\phi_{\gamma\gamma}$ are

particularly sensitive variables in the search for a fermiophobic Higgs boson.

The scalar nature of the Higgs boson affects the angular distributions of the photons in the diphoton rest frame. To minimize uncertainties from the transverse momentum of the colliding partons, the Collins-Soper frame [42] is used. In this frame, the z axis is defined as the bisector of the proton-beam momentum and the negative of the antiproton-beam momentum when they are boosted into the center-of-mass frame of the diphoton pair. The variable θ^* is defined as the angle between the leading-photon momentum and the z axis. The variable ϕ^* is defined as the angle between the diphoton plane and the $p\bar{p}$ plane. Due to the restriction to photons with $|\eta^\gamma| < 1.1$ in this analysis, the $\cos\theta^*$ distribution has little discrimination between signal and

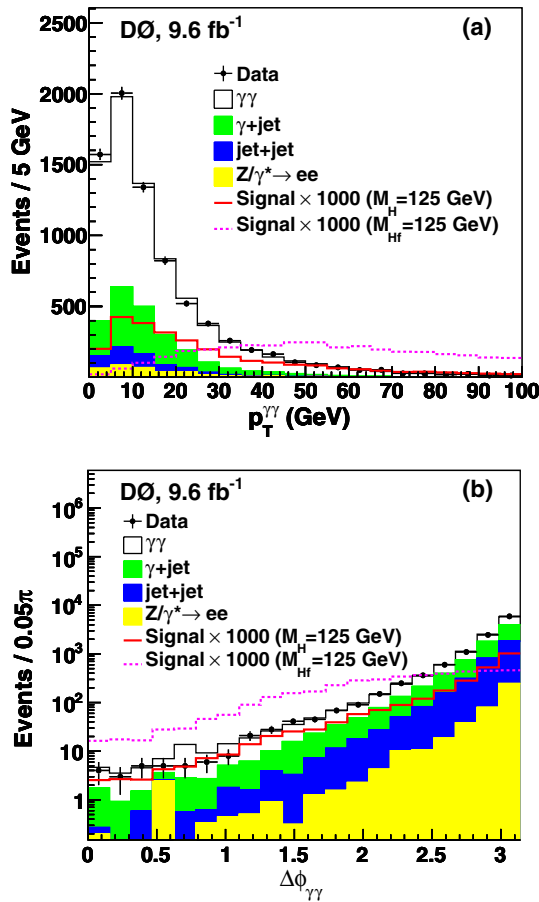


FIG. 6 (color online). Distribution of (a) $p_T^{\gamma\gamma}$ in the photon-enriched sample and (b) $\Delta\phi_{\gamma\gamma}$ in the jet-enriched sample. The data (points with statistical error bars) are compared to the background prediction, broken down into its individual components. The expected distributions for a SM Higgs boson and a fermiophobic Higgs boson with $M_H = 125$ GeV are also shown scaled by a factor of 1000. These two BDT input variables are used in both the photon-enriched and jet-enriched samples, but are displayed here for only one of the samples for illustrative purposes.

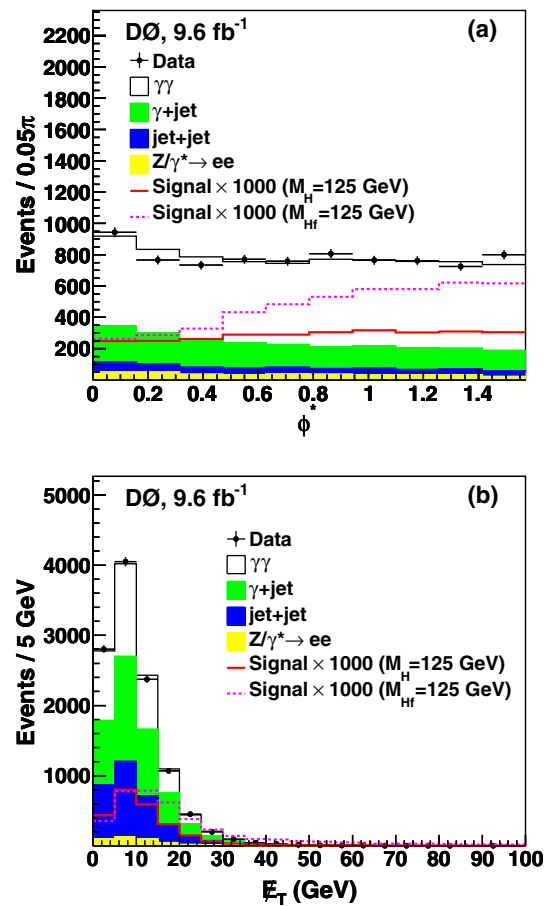


FIG. 7 (color online). Distribution of (a) ϕ^* in the photon-enriched sample and (b) \cancel{E}_T in the jet-enriched sample. The data (points with statistical error bars) are compared to the background prediction, broken down into its individual components. The expected distributions for a SM Higgs boson and a fermiophobic Higgs boson with $M_H = 125$ GeV are also shown scaled by a factor of 1000. These two BDT input variables are used in both the photon-enriched and jet-enriched samples, but are displayed here for only one of the samples for illustrative purposes.

background, although it is considered in the search. In contrast, the angle ϕ^* provides useful discrimination between signal and background, particularly for a fermiophobic Higgs boson, as illustrated in Fig. 7(a).

A significant fraction of W - and Z -boson decays in VH production involves neutrinos that result in large missing transverse energy (\cancel{E}_T) in the final state. In contrast, the \cancel{E}_T in background events is typically low, and mostly resulting from jet-energy mismeasurements. The \cancel{E}_T distribution in the jet-enriched sample is shown in Fig. 7(b). The \cancel{E}_T is reconstructed as the negative of the vectorial sum of the p_T of calorimeter cells, and is corrected for the p_T of identified muons and the energy corrections to reconstructed jets in the calorimeter [43].

Finally, the O_{NN} distributions for the leading photon ($O_{NN}^{\gamma^1}$) and the trailing photon ($O_{NN}^{\gamma^2}$) show discrimination

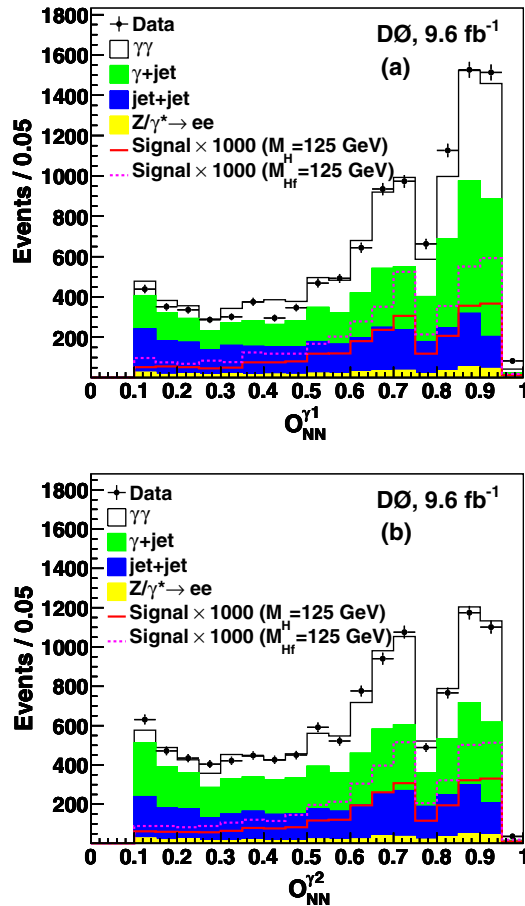


FIG. 8 (color online). Distribution of (a) $O_{NN}^{\gamma^1}$ and (b) $O_{NN}^{\gamma^2}$ in the jet-enriched sample. The data (points with statistical error bars) are compared to the background prediction, broken down into its individual components. The expected distributions for a SM Higgs boson and a fermiophobic Higgs boson with $M_H = 125$ GeV are also shown scaled by a factor of 1000. These two BDT input variables are used as well in the photon-enriched sample, although their discrimination power is limited given the $O_{NN} > 0.75$ requirement applied to both photons.

between signal and the γj and jj backgrounds, in particular in the jet-enriched sample, as illustrated in Fig. 8. The observed discrepancies between the data and the total prediction in the shape of the distribution are partly covered by the combination of statistical uncertainties on the templates and the systematic uncertainties, and they have been checked to have a negligible impact on the final result.

To improve the sensitivity of the search, a boosted-decision-tree (BDT) technique [44] is used to build a single discriminating variable combining the information from the ten variables. A different BDT is trained, for each M_H hypothesis, for events selected in the search region, corresponding to $M_{\gamma\gamma}$ falling in the interval of $M_H \pm 30$ GeV. The training is performed separately for the SM and the fermiophobic Higgs boson models, considering in each case the sum of all relevant signals against the sum of all backgrounds. A separate BDT is trained in the

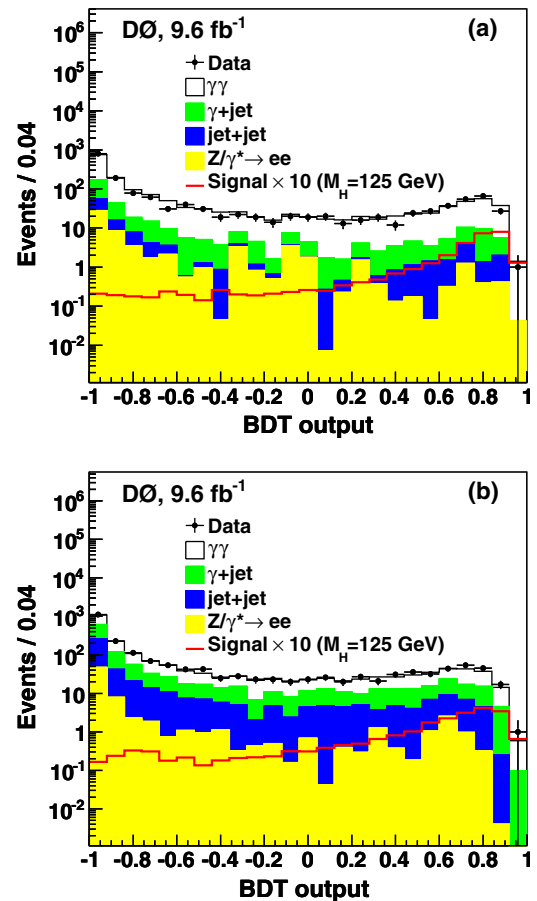


FIG. 9 (color online). Distribution of the BDT output used in the SM Higgs boson search in (a) the photon-enriched sample and (b) the jet-enriched sample. The data (points with statistical error bars) are compared to the background prediction, broken down into its individual components. The expected distributions for a SM Higgs boson with $M_H = 125$ GeV are also shown scaled by a factor of 10.

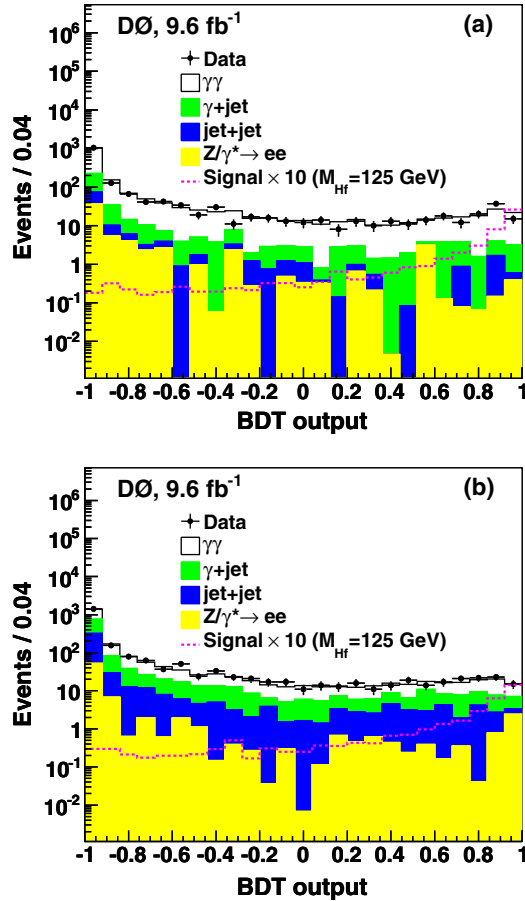


FIG. 10 (color online). Distribution of BDT output used in the fermiophobic Higgs boson search in (a) the photon-enriched sample and (b) the jet-enriched sample. The data (points with statistical error bars) are compared to the background prediction, broken down into its individual components. The expected distributions for a fermiophobic Higgs boson with $M_{H_i} = 125$ GeV are also shown scaled by a factor of 10.

photon-enriched and jet-enriched samples, respectively. The resulting BDT output distributions assuming a SM and a fermiophobic Higgs boson with $M_H = 125$ GeV are shown in Figs. 9 and 10, respectively. Prior to fitting the background yields to the data, these distributions are well modeled by the simulation and no significant excess above the background prediction is observed at high values of the BDT output.

VII. SYSTEMATIC UNCERTAINTIES

Systematic uncertainties affecting the normalization and shape of the BDT output distributions are estimated for both signal and backgrounds, taking into account correlations. Experimental uncertainties affecting the normalization of the signal and the $Z/\gamma^* \rightarrow e^+e^-$ background include the integrated luminosity (6.1%), tracking system live-time correction (2.0%), trigger efficiency

(0.1%), PV reconstruction efficiency (0.2%), and photon identification efficiency for signal (3.9%) or electron misidentification rate for $Z/\gamma^* \rightarrow e^+e^-$ (12.7%). The impact from PDF uncertainties on the signal acceptance is 1.7%–2.2% depending on M_H . Additional sources of uncertainty affecting the normalization result from uncertainties on the theoretical cross section (including variations of the renormalization and factorization scales [45] and the PDFs [46]) for signal [GF (14.1%), VH (6.2%) and VBF (4.9%)] and $Z/\gamma^* \rightarrow e^+e^-$ (3.9%) production.

The normalization uncertainties affecting the γj and jj background predictions result from propagating the uncertainties on ϵ_γ (1.5%) and ϵ_j (10%) in the estimation of their yields via Eq. (1). The uncertainties on the γj and jj yields from varying ϵ_γ are 6.9% and 5.3%, respectively. The corresponding uncertainties from varying ϵ_j are 0.6% and 15.3%, respectively.

The remaining systematic uncertainties affect the shape of the BDT output distributions. Such uncertainties include the photon energy scale (1%–5% for signal, 1%–4% for DPP background), the modeling of DPP by SHERPA (1%–10%), and the modeling of the Higgs boson p_T spectrum in GF production (1%–5%). The last two uncertainties are obtained by doubling and halving the factorization and renormalization scales with respect to the nominal choice. Uncertainties on the shape of the $\gamma j + jj$ background are 5%–7% and are estimated by comparing the BDT output distribution from the high-statistics samples obtained by inverting the O_{NN} requirement to those predicted via the matrix method.

VIII. RESULTS

For each hypothesized M_H value, the BDT output distributions discussed in Sec. VI for the photon-enriched and jet-enriched samples are used to perform the statistical analysis to search for a significant signal above the background prediction. As mentioned before, such discriminants are defined only for events with $M_{\gamma\gamma}$ falling in the $M_H \pm 30$ GeV interval. The remainder of the $M_{\gamma\gamma}$ spectrum (see Fig. 4) for both the photon-enriched and jet-enriched samples, corresponding to the sideband regions, is also included in the statistical analysis as it provides a significant constraint on the DPP normalization. Therefore, for each M_H a total of four distributions are analyzed.

In the absence of a significant data excess above the background prediction, upper limits on the product of the production cross section and branching fraction [$\sigma \times \mathcal{B}(H \rightarrow \gamma\gamma)$] are derived as a function of M_H , for both the SM and fermiophobic Higgs boson scenarios. Limits are calculated at the 95% C.L. with the modified frequentist approach [47], which employs a log-likelihood ratio (LLR) as test statistic, $LLR = -2 \ln(L_{s+b}/L_b)$, where L_{s+b} (L_b) is a binned likelihood function (product

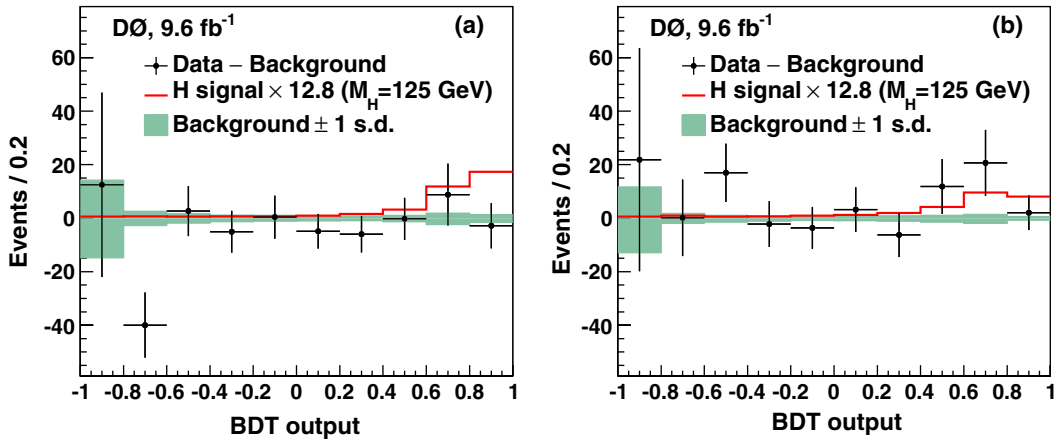


FIG. 11 (color online). Distribution of the BDT output for data (points with statistical error bars) after subtraction of the fitted background (under the background-only hypothesis) in (a) the photon-enriched sample and (b) the jet-enriched sample, for $M_H = 125$ GeV. The expected SM Higgs signal is normalized to the observed limit on $\sigma \times \mathcal{B}(H \rightarrow \gamma\gamma)$. The bands represent the 1 s.d. uncertainties on the background prediction resulting from the fit.

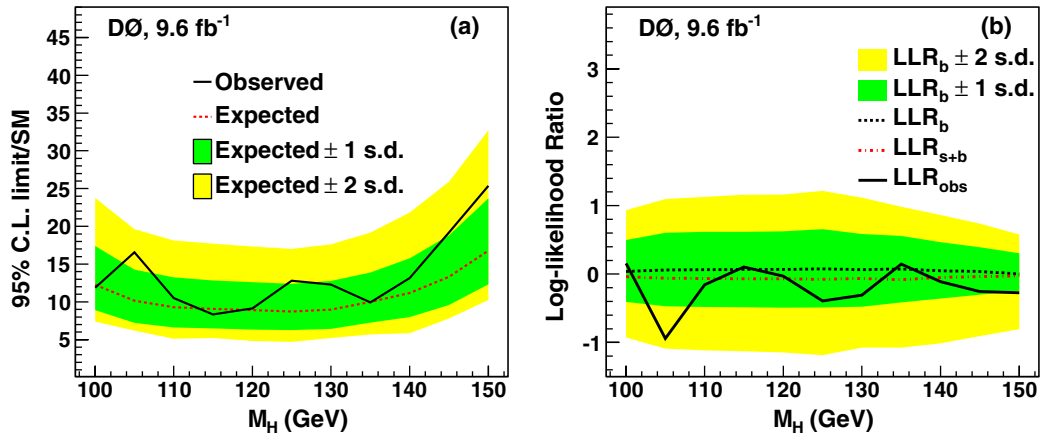


FIG. 12 (color online). (a) Observed and expected 95% C.L. limits on the ratio of $\sigma \times \mathcal{B}(H \rightarrow \gamma\gamma)$ to the SM prediction as a function of M_H . The bands correspond to 1 and 2 s.d. around the median expected limit under the background-only hypothesis. (b) Observed LLR as a function of M_H compared to the expected LLR under the background-only hypothesis (LLR_b) and signal+background hypothesis (LLR_{s+b}). The bands correspond to the 1 s.d. and 2 s.d. around the expected median LLR_b .

of Poisson probabilities) to observe the data under the signal-plus-background (background-only) hypothesis. Pseudoexperiments are generated for both hypotheses, taking into account per-bin statistical fluctuations of the

total predictions according to Poisson statistics, as well as Gaussian fluctuations describing the effect of systematic uncertainties. The individual likelihoods are maximized with respect to the DPP background

TABLE III. Expected and observed upper limits at 95% C.L. on the cross section times branching fraction for $H \rightarrow \gamma\gamma$ [$\sigma \times \mathcal{B}(H \rightarrow \gamma\gamma)$] and on $\sigma \times \mathcal{B}(H \rightarrow \gamma\gamma)$ relative to the SM prediction for a SM Higgs boson as a function of M_H .

	M_H (GeV)	100	105	110	115	120	125	130	135	140	145	150
$\sigma \times \mathcal{B}(H \rightarrow \gamma\gamma)$ (fb)	Expected	46.1	37.2	32.8	30.3	27.7	24.6	22.0	20.7	18.7	17.2	15.9
	Observed	44.7	60.6	37.1	27.9	28.4	36.1	30.1	20.5	22.0	24.8	24.0
$\sigma \times \mathcal{B}(H \rightarrow \gamma\gamma)/SM$	Expected	12.2	10.2	9.3	9.1	8.9	8.7	9.0	10.0	11.2	13.3	16.8
	Observed	11.9	16.6	10.5	8.3	9.1	12.8	12.3	9.9	13.2	19.2	25.4

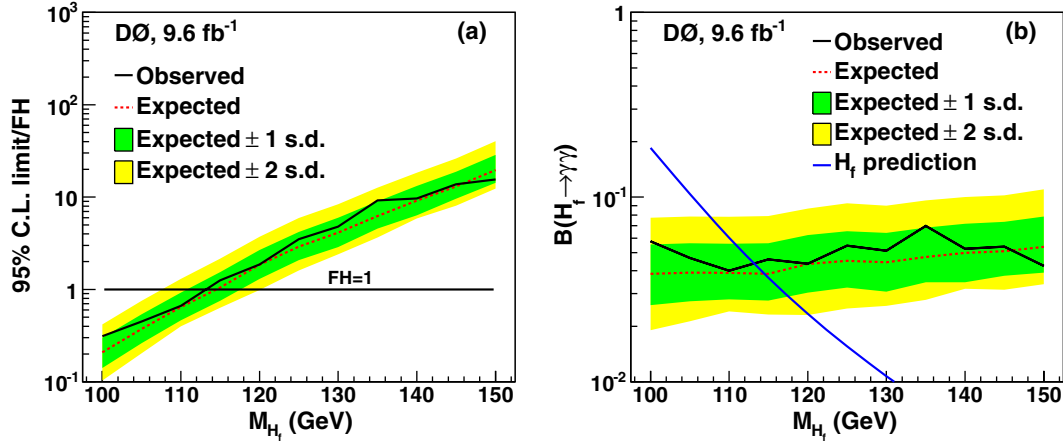


FIG. 13 (color online). (a) Observed and expected 95% C.L. limits on the ratio of $\sigma \times \mathcal{B}(H \rightarrow \gamma\gamma)$ to the fermiophobic Higgs model prediction as a function of M_{H_f} . The bands correspond to 1 and 2 s.d. around the median expected limit under the background-only hypothesis. (b) Observed and expected 95% C.L. limits on $\mathcal{B}(H_f \rightarrow \gamma\gamma)$ as a function of M_{H_f} . The bands correspond to the 1 and 2 s.d. around the median expected limit under the background-only hypothesis. Also shown is the prediction for a fermiophobic Higgs boson.

normalization as well as other nuisance parameters that parametrize the systematic uncertainties [48]. This global fit determines the normalization of the DPP background directly from data and significantly reduces the impact of systematic uncertainties on the overall sensitivity. Examples of the post-fit BDT output distribution, after background subtraction, are shown in Fig. 11. The fraction of pseudoexperiments for the signal-plus-background (background-only) hypothesis with LLR larger than a given threshold defines CL_{s+b} (CL_b). This threshold is set to the observed (median) LLR for the observed (expected) limit. Signal cross sections for which $CL_s = CL_{s+b}/CL_b < 0.05$ are deemed to be excluded at 95% C.L.

The resulting upper limits on $\sigma \times \mathcal{B}(H \rightarrow \gamma\gamma)$ relative to the SM prediction are shown as a function of M_H in Fig. 12(a), and are summarized in Table III, representing the most constraining results for a SM Higgs boson decaying into diphotons at the Tevatron.

The sensitivity of this search is approximately 50% better than that of a search based purely on the diphoton mass spectrum and not categorizing events according to the photon NN. The corresponding LLR distribution is shown in Fig. 12(b). The observed local excesses of data are under 2 s.d. and therefore are consistent with background fluctuations. At $M_H = 125$ GeV the best-fit signal cross section is a factor of 4.2 ± 4.6 above the SM prediction. At the same mass, the value of CL_{s+b} is 0.72 while the p-value for the background-only hypothesis is $1 - CL_b = 0.20$.

Upper limits on $\sigma \times \mathcal{B}(H \rightarrow \gamma\gamma)$ relative to the fermiophobic Higgs model prediction are shown as a function of M_{H_f} in Fig. 13(a), and are summarized in Table IV. This translates into the observed (expected) lower 95% C.L. of $M_{H_f} > 113$ (114) GeV. After dividing by the theoretical cross section, upper limits on $\mathcal{B}(H_f \rightarrow \gamma\gamma)$ are derived as a function of M_{H_f} and presented in Fig. 13(b).

TABLE IV. Expected and observed upper limits at 95% C.L. on the cross section times branching fraction for $H_f \rightarrow \gamma\gamma$ [$\sigma \times \mathcal{B}(H_f \rightarrow \gamma\gamma)$] and on $\mathcal{B}(H_f \rightarrow \gamma\gamma)$ for a fermiophobic Higgs boson as a function of M_{H_f} . Also given are the theoretical predictions for $\sigma \times \mathcal{B}(H_f \rightarrow \gamma\gamma)$ and $\mathcal{B}(H_f \rightarrow \gamma\gamma)$ as a function of M_{H_f} .

	M_{H_f}	100	105	110	115	120	125	130	135	140	145	150
$\sigma \times \mathcal{B}(H_f \rightarrow \gamma\gamma)$ (fb)	Expected	20.9	18.3	15.9	13.7	13.6	12.4	10.8	10.2	9.5	8.6	8.1
	Observed	31.3	22.0	16.3	16.4	13.7	15.0	12.5	15.0	10.0	9.1	6.4
	Theoretical prediction	100.4	49.0	24.7	13.1	7.3	4.3	2.6	1.6	1.0	0.7	0.4
$\mathcal{B}(H_f \rightarrow \gamma\gamma)$ (%)	Expected	3.8	3.9	3.9	3.8	4.3	4.5	4.4	4.7	5.0	5.1	5.4
	Observed	5.8	4.7	4.0	4.6	4.4	5.5	5.1	7.0	5.3	5.4	4.2
	Theoretical prediction	18.5	10.4	6.0	3.7	2.3	1.6	1.1	0.8	0.5	0.4	0.3

IX. SUMMARY

A search for a Higgs boson decaying into a pair of photons has been presented using 9.6 fb^{-1} of $p\bar{p}$ collisions at $\sqrt{s} = 1.96 \text{ TeV}$ collected with the D0 detector at the Fermilab Tevatron Collider. The search employs multivariate techniques to discriminate the signal from the non-resonant background, and is separately optimized for a SM and a fermiophobic Higgs boson. No significant excess of data above the background prediction is observed, and upper limits on the product of the cross section and branching fraction are derived at the 95% C.L. as a function of M_H . For a SM Higgs boson with $M_H = 125 \text{ GeV}$, the observed (expected) upper limits are a factor of 12.8 (8.7) above the SM prediction. The existence of a fermiophobic

Higgs boson with mass in the 100–113 GeV range is excluded at the 95% confidence level.

ACKNOWLEDGMENTS

We thank the staffs at Fermilab and collaborating institutions, and acknowledge support from the DOE and NSF (USA); CEA and CNRS/IN2P3 (France); MON, NRC KI and RFBR (Russia); CNPq, FAPERJ, FAPESP and FUNDUNESP (Brazil); DAE and DST (India); Colciencias (Colombia); CONACyT (Mexico); NRF (Korea); FOM (The Netherlands); STFC and the Royal Society (United Kingdom); MSMT and GACR (Czech Republic); BMBF and DFG (Germany); SFI (Ireland); The Swedish Research Council (Sweden); and CAS and CNSF (China).

-
- [1] S. L. Glashow, *Nucl. Phys.* **22**, 579 (1961); S. Weinberg, *Phys. Rev. Lett.* **19**, 1264 (1967); A. Salam, *Proceedings of the 8th Nobel Symposium*, edited by N. Svartholm (Almqvist and Wiksel, Stockholm, 1968), p. 367.
- [2] F. Englert and R. Brout, *Phys. Rev. Lett.* **13**, 321 (1964); P. W. Higgs, *Phys. Rev. Lett.* **13**, 508 (1964); *Phys. Lett.* **12**, 132 (1964); G. Guralnik, C. Hagen, and T. Kibble, *Phys. Rev. Lett.* **13**, 585 (1964).
- [3] The LEP Electroweak Working Group, “Status of March 2012”, <http://lepewwg.web.cern.ch/LEPEWWG/>.
- [4] ALEPH, DELPHI, L3, and OPAL Collaborations, LEP Working Group for Higgs Boson Searches, *Phys. Lett. B* **565**, 61 (2003).
- [5] T. Aaltonen *et al.* (CDF and D0 Collaborations), this issue, *Phys. Rev. D* **88**, 052013 (2013); T. Aaltonen *et al.* (CDF Collaboration), this issue, *Phys. Rev. D* **88**, 052011 (2013); V. M. Abazov *et al.* (D0 Collaboration), *Phys. Rev. D* **88**, 052014 (2013).
- [6] T. Aaltonen *et al.* (CDF and D0 Collaborations), *Phys. Rev. Lett.* **109**, 071804 (2012); T. Aaltonen *et al.* (CDF Collaboration), *Phys. Rev. Lett.* **109**, 111802 (2012); V. M. Abazov *et al.* (D0 Collaboration), *Phys. Rev. Lett.* **109**, 121802 (2012).
- [7] ATLAS Collaboration, *Phys. Lett. B* **716**, 1 (2012).
- [8] CMS Collaboration, *Phys. Lett. B* **710**, 26 (2012); CMS Collaboration, *Phys. Lett. B* **716**, 30 (2012).
- [9] S. Mrenna and J. Wells, *Phys. Rev. D* **63**, 015006 (2000).
- [10] T. Plehn and M. Rauch, *Europhys. Lett.* **100**, 11002 (2012).
- [11] A. Heister *et al.* (ALEPH Collaboration), *Phys. Lett. B* **544**, 16 (2002); P. Abreu *et al.* (DELPHI Collaboration), *Eur. Phys. J. C* **35**, 313 (2004); P. Achard *et al.* (L3 Collaboration), *Phys. Lett. B* **568**, 191 (2003); G. Abbiendi *et al.* (OPAL Collaboration), *Phys. Lett. B* **544**, 44 (2002); A. Rosca (LEP Collaborations), *Nucl. Phys. B, Proc. Suppl.* **117**, 743 (2003).
- [12] T. Aaltonen *et al.* (CDF Collaboration), *Phys. Lett. B* **717**, 173 (2012).
- [13] V. M. Abazov *et al.* (D0 Collaboration), *Phys. Rev. Lett.* **107**, 151801 (2011).
- [14] ATLAS Collaboration, *Eur. Phys. J. C* **72**, 2157 (2012).
- [15] CMS Collaboration, *J. High Energy Phys.* **09** (2012) 111.
- [16] V. M. Abazov *et al.*, *Nucl. Instrum. Methods Phys. Res., Sect. A* **565**, 463 (2006); S. N. Ahmed *et al.*, *Nucl. Instrum. Methods Phys. Res., Sect. A* **634**, 8 (2011); M. Abolins *et al.*, *Nucl. Instrum. Methods Phys. Res., Sect. A* **584**, 75 (2008); R. Angstadt *et al.*, *Nucl. Instrum. Methods Phys. Res., Sect. A* **622**, 298 (2010).
- [17] Pseudorapidity is defined as $\eta = -\ln[\tan(\theta/2)]$, where θ is the polar angle relative to the proton-beam direction, and ϕ is the azimuthal angle in the plane transverse to the proton-beam direction.
- [18] T. Andeen *et al.*, Report No. FERMILAB-TM-2365 (2007).
- [19] T. Sjöstrand, S. Mrenna, and P. Skands, *J. High Energy Phys.* **05** (2006) 026. Version 6.409 is used.
- [20] J. Pumplin, D. R. Stump, J. Huston, H-L. Lai, P. Nadolsky, and W-K. Tung, *J. High Energy Phys.* **07** (2002) 012; D. Stump, J. Huston, J. Pumplin, W-K. Tung, H-L. Lai, S. Kuhlmann, and Joseph Francis Owens, *J. High Energy Phys.* **10** (2003) 046.
- [21] C. Anastasiou, R. Boughezal, and F. Petriello, *J. High Energy Phys.* **04** (2009) 003; D. Florian and M. Grazzini, *Phys. Lett. B* **674**, 291 (2009).
- [22] J. Baglio and A. Djouadi, *J. High Energy Phys.* **10** (2010) 064.
- [23] P. Bolzoni, F. Maltoni, S. O. Moch, and M. Zaro, *Phys. Rev. Lett.* **105**, 011801 (2010).
- [24] A. D. Martin, W. J. Stirling, R. S. Thorne, and G. Watt, *Eur. Phys. J. C* **63**, 189 (2009).
- [25] A. Djouadi, J. Kalinowski, and M. Spira, *Comput. Phys. Commun.* **108**, 56 (1998). Version 3.70 is used.
- [26] G. Bozzi, S. Catani, D. de Florian, and M. Grazzini, *Phys. Lett. B* **564**, 65 (2003); *Nucl. Phys.* **B737**, 73 (2006).
- [27] T. Gleisberg, S. Höche, F. Krauss, M. Schönherr, S. Schumann, F. Siegert, and J. Winter, *J. High Energy Phys.* **02** (2009) 007. Version 1.2.2 is used.
- [28] V. M. Abazov *et al.*, (D0 Collaboration), *Phys. Lett. B* **725**, 6 (2013).

- [29] M. L. Mangano, F. Piccinini, A. D. Polosa, M. Moretti, and R. Pittau, *J. High Energy Phys.* **07** (2003) 001. Version 2.11 is used.
- [30] V. M. Abazov *et al.*, (D0 Collaboration), *Phys. Rev. Lett.* **100**, 102002 (2008).
- [31] R. Hamberg, W. L. van Neerven, and T. Matsuura, *Nucl. Phys.* **B359**, 343 (1991); *Nucl. Phys.* **B644**, 403(E) (2002).
- [32] R. Brun and F. Carminati, CERN Program Library Long Writeup Report No. W5013, 1993.
- [33] V. M. Abazov *et al.* (D0 Collaboration), *Phys. Lett. B* **659**, 856 (2008).
- [34] V. M. Abazov *et al.* (D0 Collaboration), *Phys. Rev. Lett.* **102**, 231801 (2009).
- [35] V. M. Abazov *et al.* (D0 Collaboration), *Phys. Lett. B* **653**, 378 (2007).
- [36] V. M. Abazov *et al.* (D0 Collaboration), *Nucl. Instrum. Methods Phys. Res., Sect. A* **620**, 490 (2010).
- [37] R. E. Kalman, *J. Basic Eng.* **82**, 35 (1960).
- [38] S. Kesisoglou, Brown University, Ph.D. thesis [Report No. FERMILAB-THESIS-2004-44, UMI-31-74625, 2004].
- [39] J. E. Gaiser, Ph.D. thesis, SLAC-R-255, 1982.
- [40] D. Acosta *et al.* (CDF Collaboration), *Phys. Rev. Lett.* **95**, 022003 (2005).
- [41] V. M. Abazov *et al.*, (D0 Collaboration), *Phys. Lett. B* **690**, 108 (2010).
- [42] J. C. Collins and D. E. Soper, *Phys. Rev. D* **16**, 2219 (1977).
- [43] G. C. Blazey *et al.*, [arXiv:hep-ex/0005012](https://arxiv.org/abs/hep-ex/0005012); V. M. Abazov *et al.* (D0 Collaboration), *Phys. Rev. D* **85**, 052006 (2012). Calorimeter jets are reconstructed using the iterative mid-point cone algorithm with radius $\mathcal{R} = 0.5$ in y - ϕ space, where y is the rapidity.
- [44] A. Hoecker *et al.*, Proc. Sci., ACAT (2007) 040 [[arXiv:physics/0703039](https://arxiv.org/abs/hep-ex/0703039)].
- [45] I. W. Stewart and F. J. Tackmann, *Phys. Rev. D* **85**, 034011 (2012).
- [46] S. Alekhin *et al.*, [arXiv:1101.0536](https://arxiv.org/abs/1101.0536); M. Botje *et al.*, [arXiv:1101.0538](https://arxiv.org/abs/1101.0538).
- [47] T. Junk, *Nucl. Instrum. Methods Phys. Res., Sect. A* **434**, 435 (1999); A. Read, *J. Phys. G* **28**, 2693 (2002).
- [48] W. Fisher, Report No. FERMILAB-TM-2386-E, 2006.